



Research Article

Atomic scale structure dominated FCC and B2 responses to He ion irradiation in eutectic high-entropy alloy AlCoCrFeNi_{2,1}Jingyu Pang^{a,b}, Ting Xiong^c, Wenfan Yang^{a,b}, Hualong Ge^{a,b}, Xiaodong Zheng^{a,b}, Miao Song^d, Hongwei Zhang^a, Shijian Zheng^{a,e,*}^a Institute of Metal Research, Chinese Academy of Sciences, 7, Shenyang 110016, China^b School of Material Science and Engineering, University of Science and Technology of China, Shenyang 110016, China^c Ji Hua Laboratory, Foshan 528251, China^d School of Nuclear Science and Engineering, Shanghai Jiao Tong University, Shanghai 200240, China^e State Key Laboratory of Reliability and Intelligence of Electrical Equipment, Hebei University of Technology, Tianjin 300130, China

ARTICLE INFO

Article history:

Received 10 February 2022

Revised 25 March 2022

Accepted 1 April 2022

Available online 15 May 2022

Keywords:

High-entropy alloy

AlCoCrFeNi_{2,1}

He ion irradiation

Radiation tolerance

Electron microscopy

ABSTRACT

Radiation-tolerant materials are widely desired in nuclear reactors. High-entropy alloys (HEAs) exhibiting superior mechanical performance and swelling tolerance are being considered as next-generation nuclear structural materials. However, an understanding of HEAs irradiation tolerance at an atomic scale is still lacking. In this study, the atomic scale irradiation response of AlCoCrFeNi_{2,1}, composed of face-centered cubic (FCC) phase and B2 phase, has been systematically investigated at 298 and 723 K. The bubble volume ratio of the B2 phase is much larger than that of the FCC phase under the same irradiation conditions, and hence, the FCC phase has superior swelling tolerance than the B2 phase. Also, order-disorder transformation occurred in both L1₂ and B2 phases. The different irradiation responses between the FCC and B2 phases, depend firstly on composition and secondly on crystal structure. The higher compositional complexity and complicated atomic-level lattice environment of the FCC phase contribute to better radiation performance than B2 phase. The results pave a way for exploring radiation-tolerant structural high-entropy alloys.

© 2022 Published by Elsevier Ltd on behalf of The editorial office of Journal of Materials Science & Technology.

1. Introduction

High-performance structural materials are critical for the safe operation of advanced nuclear reactors, where the neutron damage level could approach 200 displacements per atom (dpa) [1–3]. Irradiation-induced point defects generated by fast-neutron irradiation (interstitials and vacancies) and insoluble helium (He) atoms, as a byproduct of the (n, α) transmutation reaction, can accumulate to form clusters, bubbles and voids [1,4–7]. The irradiation damage can significantly degrade the structural stability and mechanical properties of nuclear materials through accelerating irradiation-induced swelling, creep, hardening and embrittlement [1,8–10]. Hence, there is substantial scientific and engineering interest in the design of intrinsically radiation-tolerant structural materials.

Recently, high-entropy alloys (HEAs) comprising five or more elements in equiatomic or near-equiatomic proportions have gar-

nered attention. Such materials are often present in face-centered cubic (FCC) and body-centered cubic (BCC) crystalline structures, and crystallize as single or double phases with a unique but simple structure [11–16]. At the atomic scale, because of the complicated and random distribution of elements and the intricate local chemical environment, HEAs have superior properties, such as high thermal stability, toughness, high-temperature strength, and good corrosion resistance, compared with conventional alloys [14,17–20]. In addition, severe lattice distortion and compositional complexity in HEAs effectively reduce the electron mean free path, and thus, reduce thermal conductivity. This structure also alters the defect dynamics, which may result in fewer irradiation-induced defects [5,6,21]. Overall, compositional complexity and lattice distortion can modify formation energies, migration barriers, and diffusion pathways of irradiation-induced defects, and hence, suppress defect accumulation [22–25]. These advantageous physical and mechanical characteristics suggest that HEAs are promising potential candidates for radiation-tolerant structural material applications.

Extensive studies have evaluated the irradiation resistance of HEAs, focusing on comparing the phase and dimension stability between HEAs and traditional alloys. For example, CrMnFeCoNi

* Corresponding author at: Institute of Metal Research, Chinese Academy of Sciences, 7, Shenyang 110016, China.

E-mail address: sjzheng@hebut.edu.cn (S. Zheng).

HEA, with a single FCC phase, exhibits enhanced radiation tolerance through the suppression of void formation, and, at elevated temperatures, has 40 times higher swelling tolerance than that of nickel [6,23,26]. The He bubble size (4.0 nm) formed in CrMnFeCoNi is considerably smaller than that (5.5 nm) seen in commercial 304 stainless steel (304SS) at 723 K irradiation [26]. With increasing Al contents, the structures of $\text{Al}_x\text{CoCrFeNi}$ HEAs evolve from FCC to FCC + BCC, and on to BCC, and show exceptional structural stability and volume swelling resistance compared with conventional nuclear materials [27,28]. Studies have shown that HEAs have superior irradiation resistance compared with traditional alloys, especially in terms of dimensional stability. The compositional complexity of HEAs is considered the primary reason for their excellent radiation resistance [5,6,23]. Compositional complexity is also reflected in a high degree of disorder, that is, mixing entropy. High mixing entropy is one of the intrinsic physical properties of HEAs, and it profoundly affects materials' performance. In $\text{Al}_x\text{CoCrFeNi}$ HEAs, Xia et al. verified that the irradiation responses of the BCC phase and FCC phase were different [28,29], but the direct comparison between lattice structure and radiation resistance has not been revealed so far. Thus, the effect of compositional complexity on the radiation performance of HEAs has not been fully explored. Consequently, there is scientific interest in understanding the roles of mixing entropy and atomic-scale lattice structure in HEAs radiation tolerance.

Recently, the $\text{AlCoCrFeNi}_{2.1}$ eutectic high-entropy alloy (EHEA), first proposed by Lu et al. [30], has drawn considerable attention because of its good combination of strength and ductility and excellent thermal mechanical properties [11,30–34]. These properties are attributed to the fine lamellar FCC and B2 dual-phase structure of $\text{AlCoCrFeNi}_{2.1}$ EHEA. The ordered B2 phase with NiAl (*cP*-CsCl type) crystal structure usually forms in Al-containing HEAs because of large negative mixing enthalpy and atomic size difference between Al and Fe, Co and Ni elements [35,36]. The mixture of soft and hard phases ensures simultaneous ductility and strength. Consequently, $\text{AlCoCrFeNi}_{2.1}$ EHEA is an ideal material for investigating the effects of compositional complexity and lattice structure under the same irradiation conditions. In this study, the $\text{AlCoCrFeNi}_{2.1}$ EHEAs were irradiated under the same conditions at both 298 K and 723 K. The FCC phase has superior swelling tolerance than that of the B2 phase in $\text{AlCoCrFeNi}_{2.1}$, owing to the higher compositional complexity and complicated atomic-level lattice environment of FCC phase. In addition, the structural evolution of the two phases of $\text{AlCoCrFeNi}_{2.1}$ has also been discussed.

2. Experiments

2.1. Material processing

The bulk alloy of eutectic $\text{AlCoCrFeNi}_{2.1}$ was prepared from commercially pure elements (Al, Co, Ni: 99.9 wt.%; Cr, Fe: approximately 99.5–99.6 wt.%). The raw elements were alloyed in a BN crucible by heating to 873 K and holding for 1 h to remove water vapor and then placed in a vacuum induction melting furnace. The furnace chamber was first evacuated to 6×10^{-2} Pa and then back-filled with high-purity argon gas to reach 0.06 MPa. The pouring temperature was 1773 K. Approximately 2.5 kg of the master alloy was melted, superheated, and poured into a MgO crucible with length of 220 mm, upper inner diameter of 62 mm, and bottom inner diameter of 50 mm. The details of alloy preparation can be found in Refs. [30,32].

2.2. Ion irradiation

Prior to irradiation, the specimens were ground using SiC grinding papers (grit 800–5000) and polished mechanically to achieve

Table 1

Chemical composition (at.%) of as-cast eutectic $\text{AlCoCrFeNi}_{2.1}$ HEA at different phases.

Phases	Al	Co	Cr	Fe	Ni
Nominal	16.39	16.39	16.39	16.39	34.42
FCC	9.04	19.41	20.77	18.53	32.23
B2	27.56	13.24	5.55	10.21	43.42

mirror-like surfaces. He ion irradiation was conducted at 298 and 723 K, using a national electrostatics corporation (NEC) ion implanter at Xiamen University. Samples were mounted on a stage with cooling and heating systems that accurately controlled the temperature. The specimens were irradiated with He ions, at a total fluence of 2×10^{17} ions/cm² over a 2 h period at 200 keV. The stopping and range of ions in matter (SRIM) simulation was used to compute the damage and resulting implanted ion concentration profiles with full-cascade mode [37], as shown in Fig. 1(a). For a eutectic structure, the compositional differences between the FCC and B2 phases are substantial. Therefore, SRIMs were run based on different FCC and B2 phase chemical compositions determined by X-ray energy-dispersive spectrometer (EDS), as shown in Table 1.

2.3. Microstructural characterization

TEM samples were prepared using a conventional cross-sectioning method, which comprised low-speed saw cutting, mechanical polishing, dimpling, and ion milling on a Gatan precision ion polishing system (PIPS) operated at 3.5 kV. Low-magnification bubble/void characterization and electron diffraction were conducted on a Tecnai G2 F30 (FEI), equipped with a high-angle angular-dark-field (HAADF) detector and an EDS system. A double Cs-corrected Titan³ G2 60–300, operated at 300 kV, was used for high-resolution HAADF scanning transmission electron microscopic (HR-HAADF-STEM) imaging.

3. Results

As shown in Fig. 1(a), the damage and He concentration peaks for the FCC phase are 19.66 dpa and 11.67 at.%, at depths of 490 and 550 nm, respectively. The equivalent values for the B2 phase are 17.82 dpa and 11.75 at.%, at depths of 540 and 600 nm, respectively. Interestingly, the damage and He concentration peaks for the B2 phase occur at deeper depths than those of the FCC phase. As shown in Fig. 1(b), the 298 K irradiation damage band is in line with the SRIM calculation with full-cascade mode, and it shows that the damage band in the B2 phase is deeper than that in the FCC phase. The surface of the 723 K irradiated sample shown in Fig. 1(c) is highlighted by the black line, which was destroyed during the ion thinning of TEM sample preparation. To avoid the influence of the interface on the experimental results, we selected the regions of the two phases, where no interfaces were involved during ion implantation for characterization, as shown in Fig. 2.

3.1. He bubble size and distribution

Typical overviews of cross-sectional TEM samples, implanted with He ions at the two different temperatures, are shown in Fig. 2(a–d). The bubble concentration region is clearly deeper in the B2 phase than that in the FCC phase. Additionally, for both phases, the bubble concentration region irradiated at 723 K is much larger than that irradiated at 298 K. The results indicate that the size and distribution of the He bubble are significantly influenced by the irradiated temperature.

To further investigate the different 298 K irradiation responses between the FCC and B2 phases, the bubble concentration region

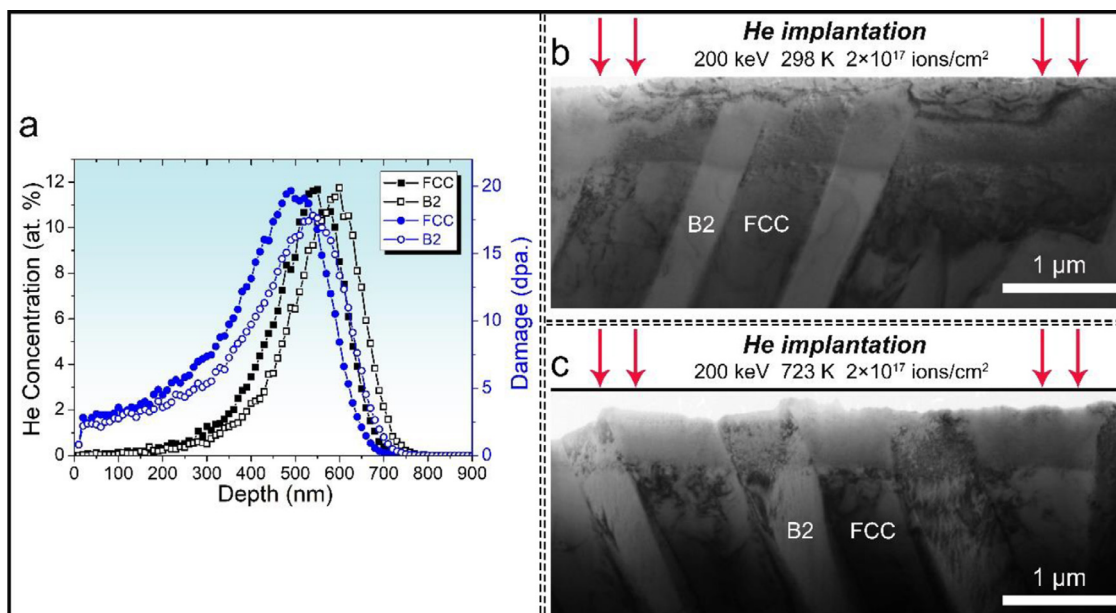


Fig. 1. (a) SRIM simulation of He ion irradiation damage and He concentration with depth for FCC and B2 phases in AlCoCrFeNi_{2.1}. Micron-scale TEM images of irradiated samples at (b) 298 K and (c) 723 K.

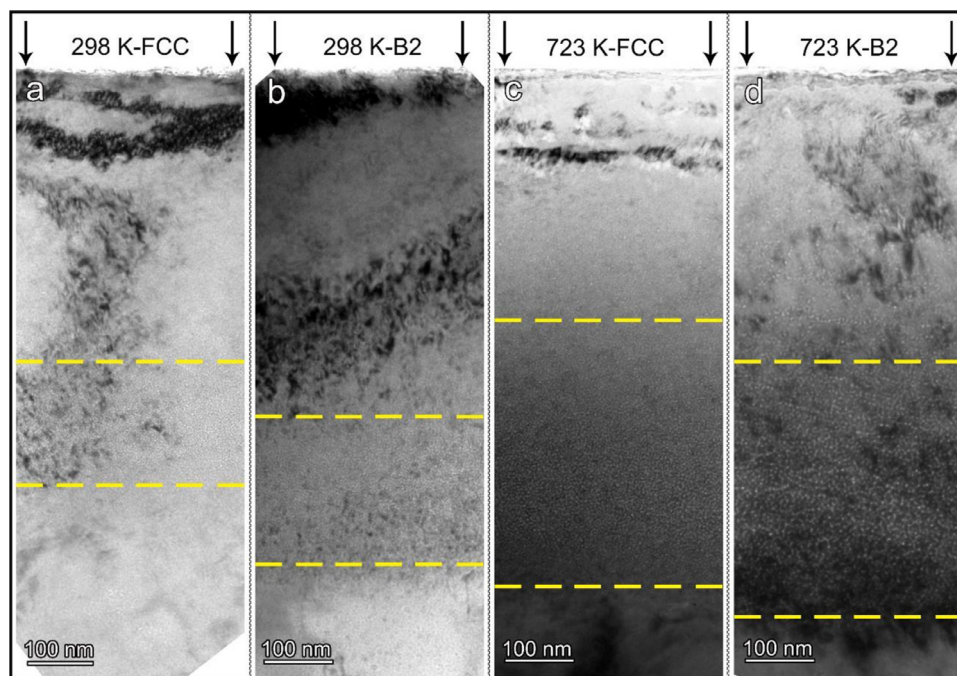


Fig. 2. Focused cross-section TEM images of AlCoCrFeNi_{2.1} samples irradiated by He ions at 298 K: (a) FCC phase, (b) B2 phase; at 723 K: (c) FCC phase, (d) B2 phase. Bubble concentration region is the area between the yellow dashed lines (For interpretation of the references to color in this figure legend, the reader is referred to the web version of this article.).

was selected to compare the bubble size, as shown in Fig. 3(a). As shown by comparing Fig. 3(b) and (c), the bubble size in the FCC phase is much smaller than that in the B2 phase. To show the bubble size distribution clearly, a statistical analysis was completed (Fig. 3(d)). The average bubble sizes (ABS) of the FCC and B2 phases are 1.21 ± 0.21 and 2.38 ± 0.50 nm, respectively, as shown in Table 2. The ratio of bubble volume ratio between B2 and FCC phase (BVR_{B2}/BVR_{FCC}) is 2.76 ± 0.51 at 298 K irradiation, where BVR_{B2} = total bubble volume/statistical region volume in B2 phase, BVR_{FCC} = total bubble volume/statistical region volume in FCC phase. Although the sample thickness (t) is unknown, it can be reduced in the subsequent calculation because the statistical bub-

Table 2

The average bubble size (ABS) and bubble volume ratio between B2 and FCC (BVR_{B2}/BVR_{FCC}) after 298 K and 723 K irradiation.

Irradiation temperature	Phase	ABS (nm)	BVR_{B2}/BVR_{FCC}
298 K	FCC	1.21 ± 0.21	2.76 ± 0.51
	B2	2.38 ± 0.50	
723 K	FCC	3.00 ± 1.01	2.70 ± 0.68
	B2	5.99 ± 1.26	

bles in the two phases are in the same region of the same sample. Thus, the FCC phase has a better anti-radiation bubble growth under 298 K irradiation.

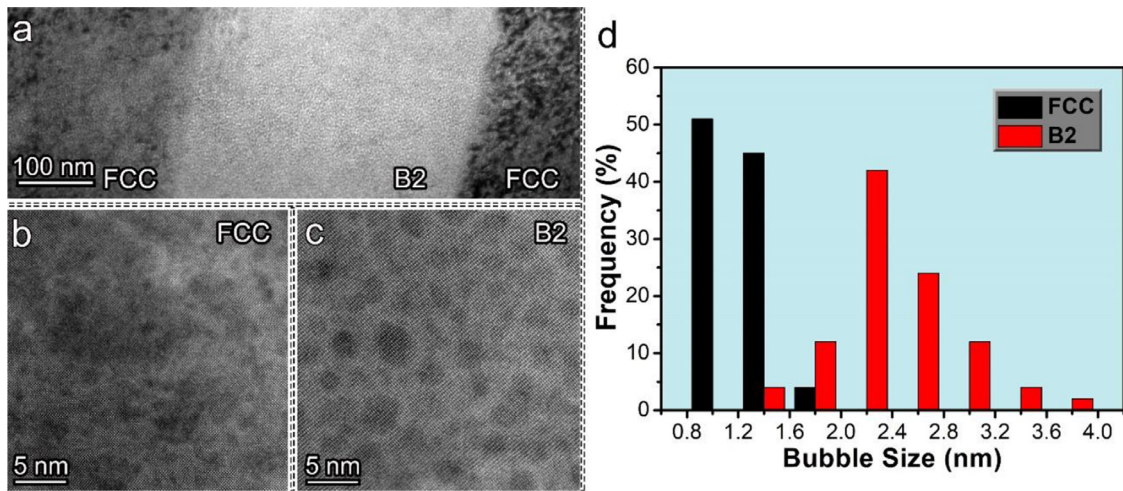


Fig. 3. Cross-section (a) TEM and HR-STEM images of (b) FCC and (c) B2 irradiated by He ions at 298 K; (d) He bubble size distribution in FCC and B2 phases at 298 K irradiation.

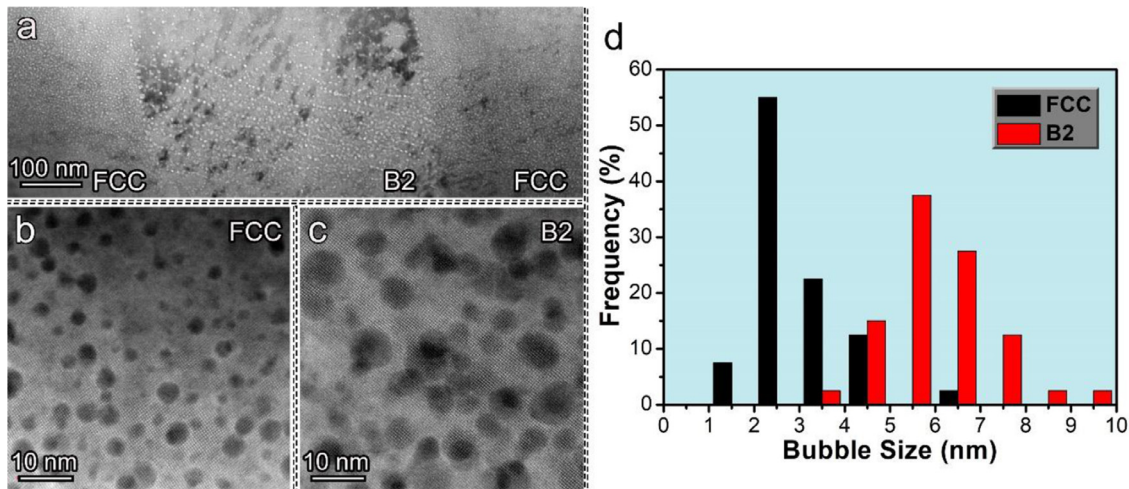


Fig. 4. Cross-section (a) TEM and HR-STEM images of (b) FCC and (c) B2 irradiated by He ions at 723 K; (d) He bubble size distribution in FCC and B2 phases at 723 K irradiation.

After 723 K irradiation, the bubble size in the FCC phase is also much smaller than that in the B2 phase, as shown in Fig. 4(a–d). The average bubble sizes of the FCC and B2 phases are 3.00 ± 1.01 and 5.99 ± 1.26 nm, respectively. With an increase in irradiated temperature, the size of the He bubbles in the B2 phase increases more quickly than those in the FCC phase. The He bubble size increments are approximately $\Delta 1.79 \pm 1.22$ and $\Delta 3.61 \pm 1.76$ nm, in the FCC and B2 phases, respectively. Additionally, the $BVR_{B2/FCC}$ at 723 K irradiation is 2.70 ± 0.68 , which is in line with the 298 K irradiation. The results indicate that in $AlCoCrFeNi_{2.1}$, the FCC phase can suppress He bubble growth more effectively than the B2 phase.

3.2. Structural evolution of FCC phase after irradiation

To reveal the irradiation-induced structural changes, electron diffraction patterns (EDPs) with an incident direction of [100] zone axis were utilized. Fig. 5 shows typical EDPs for the two phases irradiated at 298 K and 723 K. Notably, for the unirradiated FCC phase (Fig. 5(a)), weak superlattice spots (marked in red) are observed, which indicate that there is an ordered structure (nanoparticle $L1_2$ phase with Ni_3Al structure). This result is consistent with the work of Xiong et al. [38]. The weak superlattice spots do not present in the FCC phase after irradiation at 298 K and 723 K (Fig. 5(b, c)).

To investigate the disappearance of superlattice spots, dark-field (DF) TEM images were taken (Fig. 6(a–c)), which show bright points corresponding to the $L1_2$ nanoparticles. The quantity of $L1_2$ nanoparticles has clearly decreased after irradiation at 298 K and 723 K (Fig. 6(b, c)). This indicates that most of the $L1_2$ nanoparticles have transformed into the FCC structural matrix after irradiation, and thus, the weak superlattice spots have disappeared. In addition, atomic-scale characterization of the irradiated FCC phase also shows that the $L1_2$ nanoparticles have transformed into the FCC phase, as shown in Fig. 7(a, c).

3.3. Structural evolution of B2 phase after irradiation

The irradiation-induced structural changes of the B2 phase were also investigated by EDP analysis (Fig. 5(d–f)). Regardless of the irradiation level, the EDPs of the B2 phase always show superlattice spots, which indicates that the matrix retains an ordered structure even after irradiation. This is further confirmed by the atomic-scale characterization of the irradiated B2 phase (Fig. 7(b, d)), where the atomic arrangement of the B2 phase remains ordered. Although the B2 phase remains ordered after irradiation, the long-range order degree decreases as shown in Fig. 8. The long-range order degree parameter S , which is the intensity ratio between the superlattice spots and fundamental spots, enables

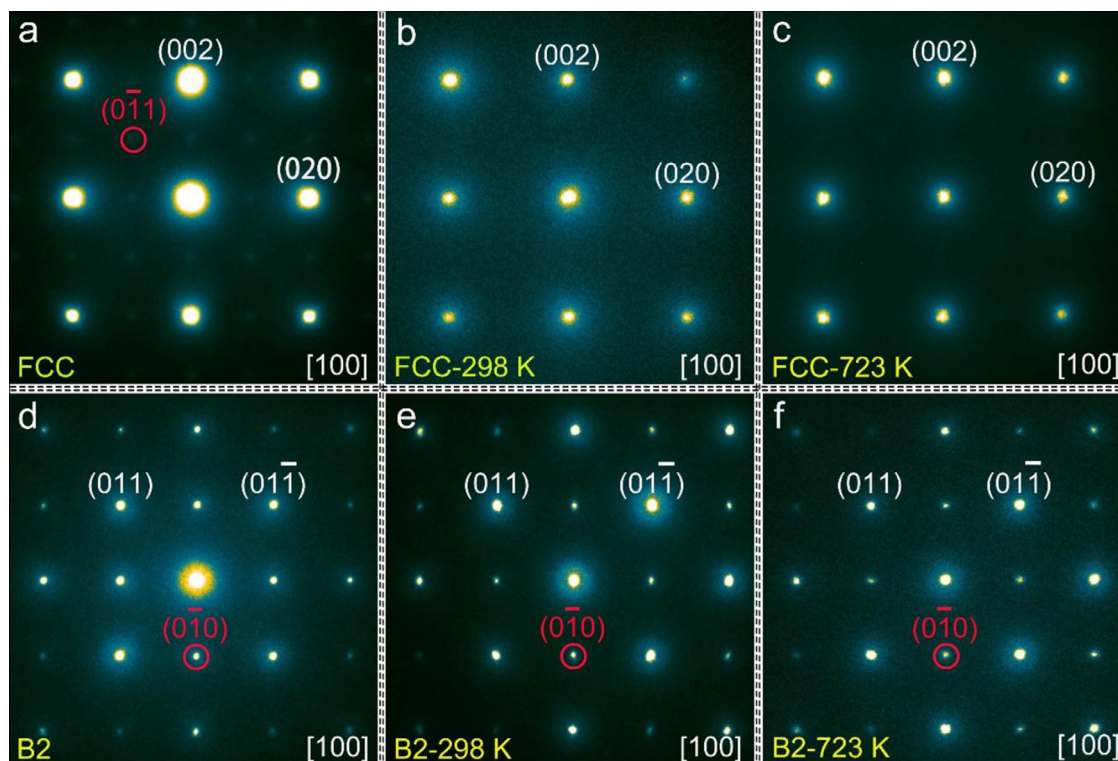


Fig. 5. Electron diffraction patterns (EDPs) of FCC (top row) and B2 phases (bottom row) before and after irradiation; (a) unirradiated, (b) 298 K irradiated, (c) 723 K irradiated of FCC phase; and (d) unirradiated, (e) 298 K irradiated, (f) 723 K irradiated of B2 phase. Red indices represent the superlattice spots.

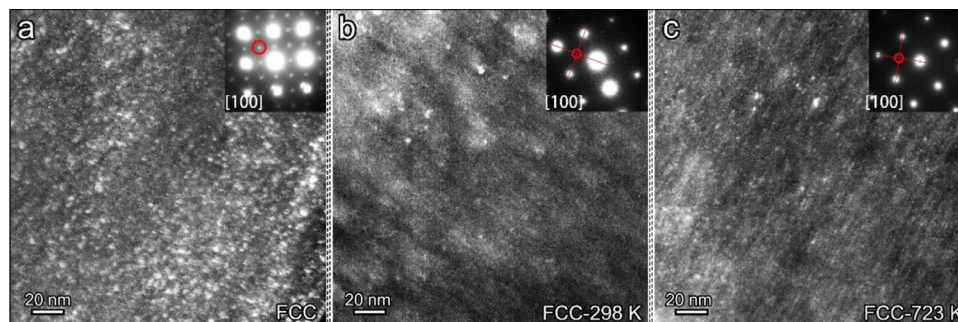


Fig. 6. Dark-field TEM images of L_{12} phases in FCC for: (a) unirradiated, (b) 298 K irradiated, and (c) 723 K irradiated. The bright contrast points are the L_{12} particles. The red circles represent the selected area of the objective aperture, with the superlattice spots.

to directly compare the order degrees acquired under different irradiations [39,40]. Consequently, the auto-correlated EDPs of the B2 phase shown in Fig. 8 have been used to reveal the changes caused by irradiation. The intensity of transmission spots, which is the fundamental spot intensity after normalization calculations by DM software, is set as 1.0. Then the intensity of superlattice spots highlighted by blue triangles in Fig. 8(a–f) are corresponding to the normalized long-range order degree. Before irradiation, the intensity of long-range order degree is approximately 0.47, and approximately 0.22 and 0.24 after irradiation at 298 K and 723 K, respectively. Although the ordered structure of the B2 phase does not completely transform to disordered BCC, the long-range order degree of the B2 phase decreased due to the irradiation.

3.4. Composition and phase transition analysis of the B2 phase after irradiation

Fig. 9(a–c) show the EDS mappings of Al, Co, Cr, Fe, and Ni elements in B2 phase. For B2 phase, the initial component distri-

butions (Fig. 9(a)) agree well with the work of Wani et al. [31]. Notably, there are many Cr-rich nanoparticles in the unirradiated B2 phase (Fig. 9(a)). These have been identified as disordered BCC nano-precipitates, presumably due to spinodal decomposition originating from compositional modulations [31,41,42]. The Cr-rich nanoparticles developed significantly after irradiation, especially for the 298 K irradiated (Fig. 9(b) Cr-K image) sample. This agrees with the reduction of order degree in the B2 phase, as analyzed quantitatively in Fig. 8. During the irradiation process, the growth of Cr-rich nanoparticles, whose structure is BCC, plays a key role in the reduction of the order degree in the B2 phase.

4. Discussion

4.1. He bubble size and distribution

The bubble size can be affected by various factors, such as irradiation temperature, dose, composition and lattice structure [43–46]. The different responses of the FCC and B2 phases un-

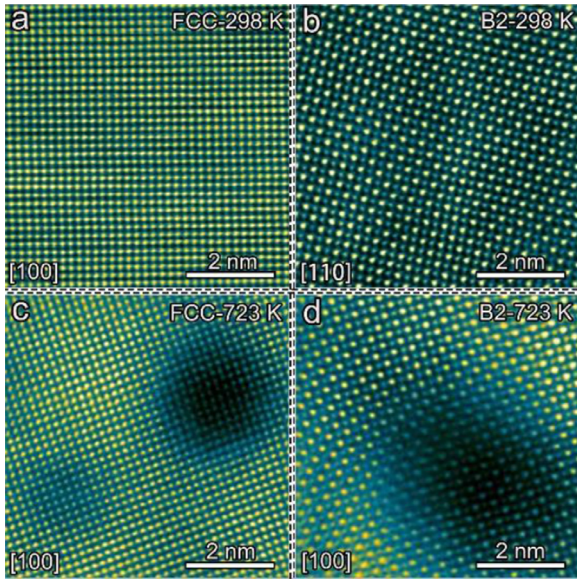


Fig. 7. IFFT mode of HR-HAADF-STEM images for FCC and B2 phases after irradiation: (a) FCC phase after 298 K irradiation, (b) B2 phase after 298 K irradiation, (c) FCC phase after 723 K irradiation, (d) B2 phase after 723 K irradiation. The dark spaces in the images are He bubbles after irradiation.

der the same irradiation conditions can be attributed to differences in composition complexity and lattice structure. The mixing entropies of FCC and B2 phases in $\text{AlCoCrFeNi}_{2.1}$ are ~ 12.89 and $\sim 11.56 \text{ J K}^{-1} \text{ mol}^{-1}$, respectively. The configurational entropy of mixing is acquired from the equation: $\Delta S_{\text{mix}} = -R \sum_i c_i \cdot \ln c_i$ [47].

Consequently, from the perspective of mixing entropy, the FCC phase will therefore show better irradiation performance than the B2 phase.

The average He bubble sizes in the FCC phase were 1.21 ± 0.21 and $3.00 \pm 1.01 \text{ nm}$, when irradiated at 298 K and 723 K, respectively. While the bubble sizes of commercial 304SS under the same irradiation conditions were ~ 2 and $5.3 \pm 1.0 \text{ nm}$, respectively [26]. Thus, the FCC phase in $\text{AlCoCrFeNi}_{2.1}$ is a better inhibitor of bubble coarsening than 304SS. The commercial 304SS, whose mixing entropy is $\sim 7.70 \pm 0.40 \text{ J K}^{-1} \text{ mol}^{-1}$, is currently used as the core internals for light water reactors [2]. However, for the B2 phase in $\text{AlCoCrFeNi}_{2.1}$, irradiated at 298 K and 723 K, the average He bubble sizes are 2.38 ± 0.50 and $5.99 \pm 1.26 \text{ nm}$, respectively. These values are larger than bubbles in 304SS under the same irradiation conditions. Therefore, the low-entropy commercial 304SS shows a better ability for restraining bubble growth than the high-entropy B2 phase in $\text{AlCoCrFeNi}_{2.1}$. Meanwhile, different from the irradiation response between FCC and B2 phase in $\text{AlCoCrFeNi}_{2.1}$, the BCC ferritic shows much less swelling than FCC austenitic [4,48]. Hence, the irradiation performance of the high-entropy B2 phase cannot be explained solely in terms of mixing entropy.

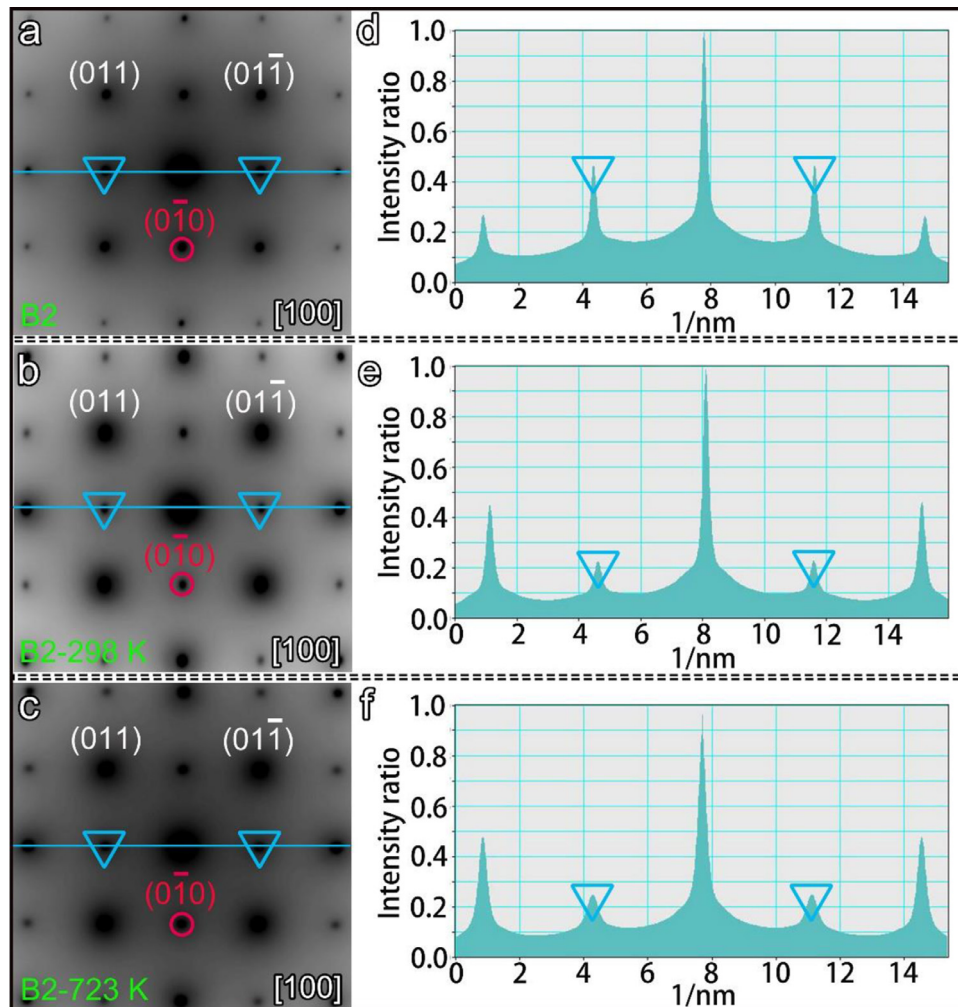


Fig. 8. Inverted and auto-correlated EDPs and relative order degree profiles of the B2 phase when: (a, d) unirradiated, (b, e) 298 K irradiated and (c, f) 723 K irradiated.

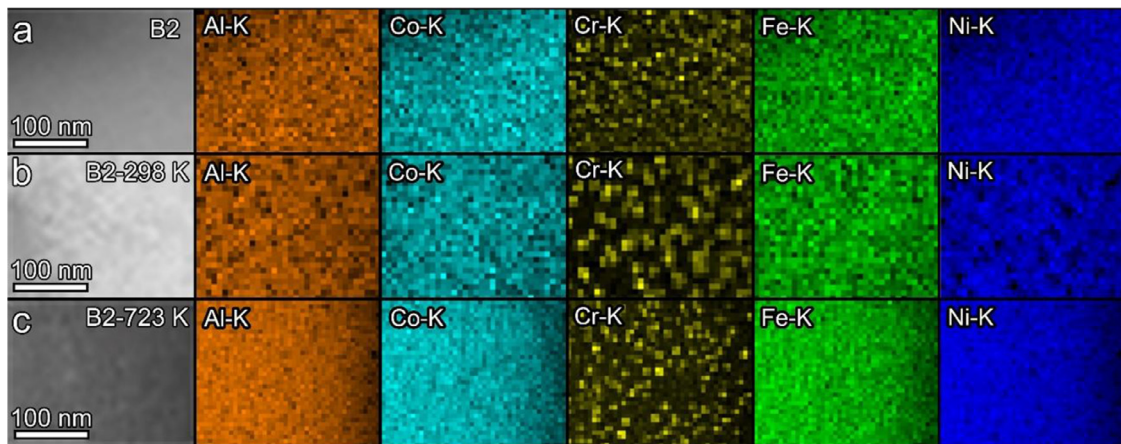


Fig. 9. EDS maps of B2 phase showing the distribution of Al, Co, Cr, Fe, Ni. (a) unirradiated, (b) 298 K irradiated, and (c) 723 K irradiated. The EDS analysis focused on bubble concentration regions.

The compositional complexity is usually divided into the numbers and types [23]. As mentioned above, the number complexity (mixing entropy) of B2 phase in AlCoCrFeNi_{2.1} is much higher than that in commercial 304SS, but its radiation resistance is still not as good as commercial 304SS, which indicates that the types of elements also have a significant impact on bubble coarsening tolerance. Jin et al. [23] have proved that alloying with Fe has a stronger influence on swelling reduction than alloying with Co and Cr. This is also in line with the results of the response of austenite and ferrite to He ion irradiation, where ferrite has better swelling tolerance under high irradiation damage. Because ferrite contains higher Fe content. Although many scholars also attributed it to the BCC structure of ferrite, the physical mechanism for the generally superior radiation resistance of BCC materials has not been fully understood [4].

The atomic-level structure also plays a key role in the material's radiation performance. A complicated atomic-level chemical environment could reduce the mean free path of interstitials in FCC HEAs, such as NiCoFeCoMn [6,26] and NiCoFeCoPd [49,50]. Additionally, chemical disorder and lattice distortion have an enormous impact on defect dynamics. Through substantial modification of the energy dissipation pathways [5], the defect diffusion is controlled by three-dimensional (3D) short-range migration [6]. The lower diffusion rate of point defects (vacancies and interstitials) in the FCC phase significantly restrains the swelling. In addition, the suppression effect on bubble growth in the FCC phase is presumably due to the high defect migration energy barrier between adjacent atoms [49]. Because a high energy barrier not only decreases the mobility of point defects but also provides effective trapping for the annihilation of freely migrating defects [6,51,52].

In contrast to the FCC phase, the B2 ordered phase has an ordered atomic arrangement, and its degree of chemical disorder is much lower. Hence, the cascade collisions caused by He ion irradiation tend to progress in the direction of the ordered atoms, since the energy barrier in that direction is minimal. Additionally, the interstitial clusters generated during cascade collisions can migrate a long distance easily along the glide cylinder with one dimensional (1D) migration, leaving a high-vacancy supersaturation behind to be susceptible to detrimental bubble formation [6]. Thus, the He bubbles in the B2 phase distribute in a specific array at 723 K as shown in Fig. 4(a), which indicates that 1D migration channels promote the growth of He bubbles. The response of the B2 phase to He ions irradiation needs to be further explored, especially when the He bubbles grow up in a specific orientation under 723 K irradiation.

4.2. Order-disorder transformation

4.2.1. Disorder of L1₂ phase

The disordering of the L1₂ phase is an interesting feature of the irradiation response of the FCC phase in AlCoCrFeNi_{2.1}. This disordering phenomenon has been shown in AlCoCrFeNi_{2.1} with severe cold-rolling and L1₂-Ni₃Al subjected to high-pressure torsion, ball milling, and electron irradiation [31,39,53–55]. The dislocation activities alone could not account for the disordering, and the contributions of microbands and shear bands are more important. Thus, severely localized deformation plays a key role in the disordering process of the L1₂ phase in AlCoCrFeNi_{2.1} [31,53]. In terms of He ion irradiation, the high-energy He ion injection plays a crucial role in the disordering of the L1₂ phase.

Firstly, He ion irradiation can supply the energy necessary to induce transformations from the equilibrium to higher-energy metastable states, such as ordered to disordered, ordered to amorphous [56–58]. Point defects (vacancies and interstitials), interstitial clusters, He-vacancy clusters, and dislocations are all the result of damage defects induced by He ion irradiation. These raise the free energy of the matrix and provide the driving force needed for the transformation from the L1₂ phase to the FCC phase [56].

Secondly, the disordering of L1₂ phase is attributed to ballistic mixing or atomic mixing by replacement collision sequences [59]. Within the L1₂ particles, the change of long-range order parameter *S* during irradiation is expressed as [60]:

$$\frac{dS}{dt} = \left(\frac{dS}{dt} \right)_{\text{irr}} + \left(\frac{dS}{dt} \right)_{\text{thermal}}$$

where the first term is chemical disorder induced by defect production processes, lasting a few picoseconds; while the second term refers to the thermal reordering toward equilibrium by diffusion processes. For a high temperature ($T \geq 0.6T_m$) irradiation, the thermal equilibrium vacancy concentration is large, and thus the irradiation-induced defects can be annihilated quickly because of the thermal reordering toward equilibrium owing to a high diffusion rate [61]. However, irradiation-produced defects dominate the diffusion process at 723 K ($T = 0.45T_m$) irradiation in this study, which means that the thermal diffusion is kinetically inhibited. Therefore, the irradiation-induced disorder is significant in L1₂. While similar phenomena have been frequently observed in the other alloys, such as disorder of γ'' phase (D0₂₂) and γ' phase (L1₂) in Ni-based alloy during ion irradiation [62,63].

4.2.2. Order degree reduction of B2 phase

According to the composition data in Table 1, the B2 phase is depleted in Cr but enriched in Al and Ni. In combination with Fig. 7(b, d), it can be determined that the B2 structure also contains Co and Fe and has (Ni, Co, Fe)-Al ordering, because Co and Fe have a strong affinity with Al too [35]. The calculated critical temperature of NiAl ordering-disordering transition is 6095 K, although the authors also admit the error in the critical temperature due to the inadequacy of the Bragg-Williams theory [64]. There is also an exception that NiAl probably disorders at a temperature somewhere between 1073 K and 1473 K [65]. Nonetheless, the temperature is also much higher than the irradiation temperatures in this work. Additionally, other studies have suggested that NiAl is a highly ordered phase that cannot be disordered under electron or He ion irradiation [64].

However, in the present study, the order degree of the B2 phase has reduced noticeably, which results in a decrease in the intensity of the superlattice reflections. As shown in Fig. 8, the ordering degree has decreased from 0.47 to 0.22 and 0.24 after irradiation at 298 K and 723 K, respectively. The growth of BCC nano-precipitates is the reason for the order degree reduction of the B2 phase, as shown in Fig. 9. The mechanism for the transformation from the B2 to BCC phase is in line with the disordering of L1₂ phase under He ion irradiation: the high-energy He ion injection plays a crucial role to supply the energy necessary to induce transformations from the equilibrium to higher-energy metastable states, including ordering to disordering. And the disordering of B2 phase is also attributed to ballistic mixing or atomic mixing by replacement collision sequences, in which the diffusion process is dominated by the movement of irradiation-produced defects.

5. Conclusion

In summary, in AlCoCrFeNi_{2.1}, the disordered FCC phase has a stronger ability to suppress the nucleation and growth of He bubbles than the B2 structure. Based on the investigation in detail, some key conclusions can be drawn as follows:

- (1) The bubble size of the B2 phase is much larger than that of the FCC phase under the same irradiation conditions. Therefore, the swelling tolerance of the FCC phase is superior to the B2 phase.
- (2) The disordering of L1₂ phase (L1₂ to FCC phase) and order degree reduction of B2 phase (B2 to BCC nano-precipitates) have been identified in AlCoCrFeNi_{2.1} under He ion irradiation. Both disordering and order degree reduction are dominated by high-energy He ion injection and replacement collision sequences.
- (3) The different irradiation response between FCC and B2 phases is attributed to the higher compositional complexity (numbers and types of elements) and complicated atomic-level lattice environment of the high-entropy FCC phase. The compositional complexity and atomic-scale lattice structure are both crucial factors that must be addressed simultaneously when designing advanced radiation-resistant HEAs.

Acknowledgments

This work was supported by financial support from the National Natural Science Foundation of China (Nos. 51771201 and 52071124), the Key Project of Natural Science Foundation of Tianjin (No. 20JCZDJC00440), the National Key Research and Development Program (No. 2018YFB0703402), and the Open Research Fund from the State Key Laboratory of Rolling and Automation, Northeastern University (No. 2020RALKFKT002).

Reference

- [1] S.J. Zinkle, J.T. Busby, *Mater. Today* 12 (2009) 12–19.
- [2] S.J. Zinkle, G.S. Was, *Acta Mater.* 61 (2013) 735–758.

- [3] N.A.P.K. Kumar, C. Li, K.J. Leonard, H. Bei, S.J. Zinkle, *Acta Mater.* 113 (2016) 230–244.
- [4] S.J. Zinkle, L.L. Snead, *Ann. Rev. Mater. Res.* 44 (2014) 241–267.
- [5] Y. Zhang, G.M. Stocks, K. Jin, C. Lu, H. Bei, B.C. Sales, L. Wang, L.K. Beland, R.E. Stoller, G.D. Samolyuk, M. Caro, A. Caro, W.J. Weber, *Nat. Commun.* 6 (2015) 8736.
- [6] C. Lu, L. Niu, N. Chen, K. Jin, T. Yang, P. Xiu, Y. Zhang, F. Gao, H. Bei, S. Shi, M.R. He, I.M. Robertson, W.J. Weber, L. Wang, *Nat. Commun.* 7 (2016) 13564.
- [7] Z. Fan, S. Zhao, K. Jin, D. Chen, Y.N. Osetskiy, Y. Wang, H. Bei, K.L. More, Y. Zhang, *Acta Mater.* 164 (2019) 283–292.
- [8] C. Lu, T. Yang, K. Jin, G. Velisa, P. Xiu, M. Song, Q. Peng, F. Gao, Y. Zhang, H. Bei, W.J. Weber, L. Wang, *Mater. Res. Lett.* 6 (2018) 584–591.
- [9] J.F. Stubbins, *J. Nucl. Mater.* (1986) 748–753 141–143.
- [10] Z. Chen, L.L. Niu, Z. Wang, L. Tian, L. Kecskes, K. Zhu, Q. Wei, *Acta Mater.* 147 (2018) 100–112.
- [11] I.S. Wani, T. Bhattacharjee, S. Sheikh, Y.P. Lu, S. Chatterjee, P.P. Bhattacharjee, S. Guo, N. Tsuji, *Mater. Res. Lett.* 4 (2016) 174–179.
- [12] Z. Li, K.G. Pradeep, Y. Deng, D. Raabe, C.C. Tasan, *Nature* 534 (2016) 227–+.
- [13] C. Niu, C.R. LaRosa, J. Miao, M.J. Mills, M. Ghazisaeidi, *Nat. Commun.* 9 (2018) 1363.
- [14] J. Pang, T. Xiong, X. Wei, Z. Zhu, B. Zhang, Y. Zhou, X. Shao, Q. Jin, S. Zheng, X. Ma, *Materialia* 6 (2019) 100275.
- [15] J. Pang, H. Zhang, L. Zhang, Z. Zhu, H. Fu, H. Li, A. Wang, Z. Li, H. Zhang, *J. Mater. Sci. Technol.* 78 (2020) 74–80.
- [16] Y. Wu, F. Zhang, X. Yuan, H. Huang, X. Wen, Y. Wang, M. Zhang, H. Wu, X. Liu, H. Wang, S. Jiang, Z. Lu, *J. Mater. Sci. Technol.* 62 (2021) 214–220.
- [17] B. Gludovatz, A. Hohenwarter, D. Catoor, E.H. Chang, E.P. George, R.O. Ritchie, *Science* 345 (2014) 1153–1158.
- [18] Z. Wu, H. Bei, *Mater. Sci. Eng. A* 640 (2015) 217–224.
- [19] Z. Li, K.G. Pradeep, Y. Deng, D. Raabe, C.C. Tasan, *Nature* 534 (2016) 227.
- [20] M.H. Tsai, J.W. Yeh, *Mater. Res. Lett.* 2 (2014) 107–123.
- [21] Y. Lu, H. Huang, X. Gao, C. Ren, J. Gao, H. Zhang, S. Zheng, Q. Jin, Y. Zhao, C. Lu, T. Wang, T. Li, *J. Mater. Sci. Technol.* 35 (2019) 369–373.
- [22] D.S. Aidhy, C. Lu, K. Jin, H. Bei, Y. Zhang, L. Wang, W.J. Weber, *Acta Mater.* 99 (2015) 69–76.
- [23] K. Jin, C. Lu, L.M. Wang, J. Qu, W.J. Weber, Y. Zhang, H. Bei, *Scr. Mater.* 119 (2016) 65–70.
- [24] C. Lu, K. Jin, L.K. Beland, F. Zhang, T. Yang, L. Qiao, Y. Zhang, H. Bei, H.M. Christen, R.E. Stoller, L. Wang, *Sci. Rep.* 6 (2016) 19994.
- [25] Z. Zhang, E.H. Han, C. Xiang, *J. Mater. Sci. Technol.* 84 (2021) 230–238.
- [26] L. Yang, H. Ge, J. Zhang, T. Xiong, Q. Jin, Y. Zhou, X. Shao, B. Zhang, Z. Zhu, S. Zheng, X. Ma, *J. Mater. Sci. Technol.* 35 (2019) 300–305.
- [27] S.Q. Xia, X. Yang, T.F. Yang, S. Liu, Y. Zhang, *JOM* 67 (2015) 2340–2344.
- [28] S.-q. Xia, Z. Wang, T.-f. Yang, Y. Zhang, *J. Iron Steel Res., Int.* 22 (2015) 879–884.
- [29] S. Xia, M.C. Gao, T. Yang, P.K. Liaw, Y. Zhang, *J. Nucl. Mater.* 480 (2016) 100–108.
- [30] Y. Lu, Y. Dong, S. Guo, L. Jiang, H. Kang, T. Wang, B. Wen, Z. Wang, J. Jie, Z. Cao, H. Ruan, T. Li, *Sci. Rep.* 4 (2014) 6200.
- [31] I.S. Wani, T. Bhattacharjee, S. Sheikh, P.P. Bhattacharjee, S. Guo, N. Tsuji, *Mater. Sci. Eng. A* 675 (2016) 99–109.
- [32] Y. Lu, X. Gao, L. Jiang, Z. Chen, T. Wang, J. Jie, H. Kang, Y. Zhang, S. Guo, H. Ruan, Y. Zhao, Z. Cao, T. Li, *Acta Mater.* 124 (2017) 143–150.
- [33] X. Gao, Y. Lu, B. Zhang, N. Liang, G. Wu, G. Sha, J. Liu, Y. Zhao, *Acta Mater.* 141 (2017) 59–66.
- [34] T. Xiong, W. Yang, S. Zheng, Z. Liu, Y. Lu, R. Zhang, Y. Zhou, X. Shao, B. Zhang, J. Wang, F. Yin, P.K. Liaw, X. Ma, *J. Mater. Sci. Technol.* 65 (2020) 216–227.
- [35] Y.H. Meng, F.H. Duan, J. Pan, Y. Li, *Intermetallics* 111 (2019) 106515.
- [36] J.L. Li, Z. Li, Q. Wang, C. Dong, P.K. Liaw, *Acta Mater.* 197 (2020) 10–19.
- [37] W.J. Weber, Y. Zhang, *Curr. Opin. Solid State Mater. Sci.* 23 (2019) 100757.
- [38] T. Xiong, S. Zheng, J. Pang, X. Ma, *Scr. Mater.* 186 (2020) 336–340.
- [39] H.C. Liu, T.E. Mitchell, *Acta Metall.* 31 (1983) 863–872.
- [40] G.J.C. Carpenter, E.M. Schulson, *J. Nucl. Mater.* 73 (1978) 180–189.
- [41] L.J. Santodonato, Y. Zhang, M. Feyngenson, C.M. Parish, M.C. Gao, R.J.K. Weber, J.C. Neufeld, Z. Tang, P.K. Liaw, *Nat. Commun.* 6 (2015) 5964.
- [42] W.R. Wang, W.L. Wang, S.C. Wang, Y.C. Tsai, C.H. Lai, J.W. Yeh, *Intermetallics* 26 (2012) 44–51.
- [43] H. Trinkaus, B.N. Singh, *J. Nucl. Mater.* 323 (2003) 229–242.
- [44] S.J. Zinkle, J. Steven, in: *Comprehensive Nuclear Materials*, Elsevier Ltd., 2012, pp. 65–98.
- [45] S.I. Golubov, A. Barashev, R.E. Stoller, *Compr. Nucl. Mater.* 1 (2012) 357–391.
- [46] W.T. Lin, G.M. Yeli, G. Wang, J.H. Lin, S.J. Zhao, D. Chen, S.F. Liu, F.L. Meng, Y.R. Li, F. He, Y. Lu, J.J. Kai, *J. Mater. Sci. Technol.* 101 (2022) 226–233.
- [47] Y. Zhang, T.T. Zuo, Z. Tang, M.C. Gao, K.A. Dahmen, P.K. Liaw, Z.P. Lu, *Prog. Mater. Sci.* 61 (2014) 1–93.
- [48] C. Parkin, M. Moorehead, M. Elbakshwan, J. Hu, W.Y. Chen, M. Li, L. He, K. Sridharan, A. Couet, *Acta Mater.* 198 (2020) 85–99.
- [49] T.N. Yang, C. Lu, G. Velisa, K. Jin, P. Xiu, Y. Zhang, H. Bei, L. Wang, *Scr. Mater.* 158 (2019) 57–61.
- [50] Y. Tong, G. Velisa, S. Zhao, W. Guo, T. Yang, K. Jin, C. Lu, H. Bei, J.Y.P. Ko, D.C. Pagan, Y. Zhang, L. Wang, F.X. Zhang, *Materialia* 2 (2018) 73–81.
- [51] E. Wakai, T. Ezawa, J. Imamura, T. Takenaka, T. Tanabe, R. Oshima, *J. Nucl. Mater.* (2002) 367–373 307–311.
- [52] K. Fukumoto, A. Kimura, H. Matsui, *J. Nucl. Mater.* 258–263 (1998) 1431–1436.
- [53] J. Ball, G. Gottstein, *Intermetallics* 2 (3) (1994) 205–219.
- [54] C. Rentenberger, H.P. Karnthaler, *Acta Mater.* 56 (2008) 2526–2530.
- [55] J.S.C. Jang, C.C. Koch, *J. Mater. Res.* 5 (2011) 498–510.
- [56] M. Nastasi, J.W. Mayer, *Mater. Sci. Rep.* 6 (1991) 1–51.
- [57] E.M. Schulson, *J. Nucl. Mater.* 83 (1979) 239–264.

- [58] J. Lian, L. Wang, J. Chen, K. Sun, R.C. Ewing, J.Matt Farmer, L.A. Boatner, *Acta Mater.* 51 (2003) 1493–1502.
- [59] G. Martin, *Phys. Rev. B* 30 (1984) 1424–1436.
- [60] C.R. Lear, R.S. Averback, P. Bellon, A.E. Sand, M.A. Kirk, *J. Mater. Res.* 33 (2018) 3841–3848.
- [61] J. Mayer, J.K. Hirvonen, M.R. Nastasi, in: *Ion-Solid Interactions*, Cambridge University Press, Cambridge, 1996, pp. 191–217.
- [62] C.R. Lear, M. Song, M. Wang, G.S. Was, *J. Nucl. Mater.* 516 (2019) 125–134.
- [63] C. Sun, M. Kirk, M. Li, K. Hattar, Y. Wang, O. Anderoglu, J. Valdez, B.P. Uberuaga, R. Dickerson, S.A. Maloy, *Acta Mater.* 95 (2015) 357–365.
- [64] R. Visnov, J.A. Alonso, L.A. Girifalco, *Metall. Trans. A* 11 (1980) 1747–1753.
- [65] R. Hultgren, P. Desai, D. Hawkins, M. Gleiser, K. Kelley, *Selected Values of the Thermodynamic Properties of Binary Alloys*, American Society for Metals Metal Park, 1973.